

Characteristics of Strong Ground Motions from Four $M_S \geq 5.0$ Earthquakes in the 2021 Yangbi, Southwest China, Seismic Sequence

Shengyin Qiang, Hongwei Wang, Ruizhi Wen, Yefei Ren & Jianwen Cui

To cite this article: Shengyin Qiang, Hongwei Wang, Ruizhi Wen, Yefei Ren & Jianwen Cui (2022): Characteristics of Strong Ground Motions from Four $M_S \geq 5.0$ Earthquakes in the 2021 Yangbi, Southwest China, Seismic Sequence, Journal of Earthquake Engineering, DOI: [10.1080/13632469.2022.2143941](https://doi.org/10.1080/13632469.2022.2143941)

To link to this article: <https://doi.org/10.1080/13632469.2022.2143941>



Published online: 14 Nov 2022.



Submit your article to this journal



View related articles



View Crossmark data



Characteristics of Strong Ground Motions from Four $M_S \geq 5.0$ Earthquakes in the 2021 Yangbi, Southwest China, Seismic Sequence

Shengyin Qiang  ^{a,b}, Hongwei Wang  ^{a,b}, Ruizhi Wen  ^{a,b}, Yefei Ren ^{a,b}, and Jianwen Cui^c

^aKey Laboratory of Earthquake Engineering and Engineering Vibration, Institute of Engineering Mechanics, China Earthquake Administration, Harbin, China; ^bKey Laboratory of Earthquake Disaster Mitigation, Ministry of Emergency Management, Harbin, China; ^cYunnan Earthquake Agency, Kunming, China

ABSTRACT

A seismic sequence has struck the Yangbi county, west part of Yunnan Province in southwest China since May 18, 2021. This region experienced the strongest ground shakings on the night of 21 May with the successive occurrence of four earthquakes with $M_S \geq 5.0$ in a short time and more small earthquakes. Large numbers of strong-motion recordings obtained in the four earthquakes with $M_S \geq 5.0$ (i.e. the M_S 5.6 foreshock, the M_S 6.4 mainshock, the M_S 5.0 and M_S 5.2 aftershocks) were analyzed in detail to characterize the source effects, distance decay, etc. The velocity pulse-like waveform at near-source station 53YBX and the significant asymmetry of distance decay along the SSE-NNW direction (i.e. much slower toward the SSE) in the M_S 6.4 mainshock seem to hint the occurrence of the asymmetrical source rupture. The source rupture directivity for the four events were investigated by fitting the azimuth-dependent residuals of the PGAs. The M_S 6.4 mainshock is characterized by the significantly asymmetrical bilateral rupture propagation, predominantly in the SSE direction with a rupture velocity of about 2.24 km/s. The PGA and PSAs from the four earthquakes were further compared with the predicted medians of the ASK14 and CY14 prediction models for global shallow crustal earthquakes. The negative inter-events residuals reflect the weaker source contributions of the Yangbi events to ground motions. The source contributions to short-period ground motions approximately show the dependence on earthquake type, that is, M_S 5.6 foreshock $>$ M_S 6.4 mainshock $>$ M_S 5.2 aftershock, consistent with the dependence of stress drop on earthquake type. We further noted that the inter-events values for the M_S 5.0 aftershock are far below those for the M_S 5.2 aftershock. This may be attributed to the differences in the spatial and temporal distance to the mainshock, that is, weak source contributions from the close aftershocks to the mainshock. The values of adjustment coefficient Δc_3 are almost positive, indicating the weaker anelastic attenuations in the study region. Finally, we also found that the distance scaling of significant duration can be well described by both empirical models (AS16 model for predicting significant duration and the BT14 model for empirically illustrating the ground-motion path duration).

ARTICLE HISTORY

Received 17 March 2022
Accepted 31 October 2022

KEYWORDS

2021 Yangbi earthquake;
strong ground motion;
rupture directivity; source
effect; distance decay

1. Introduction

Since May 18, 2021, a series of small-to-moderate earthquakes with surface magnitudes (M_S) smaller than 5.0 have successively shook the Yangbi County located in the west part of Yunnan Province in southwest China. The strongest seismicity was aroused on May 21 as the largest magnitude earthquake

(M_S 6.4) occurred at 21:48:34 local time, which was closely preceded by three moderate foreshocks (M_S 4.2, 5.6, 4.5 in chronological order) just one hour ago and moreover was followed by six aftershocks with M_S not smaller than 4.0 one hour later. Up until May 28, the Yangbi seismic sequence comprises of 45 events with $M_S \geq 3.0$, primarily nucleated at shallow crust with a depth of 8–12 km as reported by the China Earthquake Network Center (CENC). It is a typical foreshock-mainshock-aftershock seismic sequence. After the M_S 6.4 mainshock, the macroseismic intensity map was released and the maximum in the epicentral area reaches VIII on the Chinese seismic intensity scale (http://yndzj.gov.cn/yndzj/_300559/_300651/629959/index.html). Numerous casualties and property losses were caused by successive earthquakes and their induced geological disasters (https://www.mem.gov.cn/xw/bndt/202105/t20210522_385746.shtml).

The M_S 6.4 mainshock has a shallow focal depth of 8 km and epicenter at 25.67°N, 99.87°E according to CENC. It is approximately located at the northwesternmost extent of this sequence, about 6.7 km northwest to the epicenter of the largest magnitude foreshock (M_S 5.6) (Fig. 1). The largest magnitude aftershock (M_S 5.2) is approximately located at the southeast end of the sequence, while the second largest aftershock (M_S 5.0) is very close to the mainshock (Fig. 1). The mainshock is a typical strike-slip event with very high dip angle and its moment magnitude (M_w) is measured at 6.1 according to the focal mechanism solution (i.e. strike/dip/rake = 314°/83°/170°) derived from the Global Centroid Moment Tensor (CMT) catalog. However, both the M_S 5.6 foreshock and the M_S 5.2 aftershock share the normal-faulting mechanisms with the left-lateral strike-slip component.

The Yangbi seismic sequence is spatially extended by a length of about 20 km approximately along a northwest-southeast-trending blind branch fault parallel to the right-lateral strike-slip Weixi-Qiaohou fault on the east side (Duan et al. 2021; Li et al. 2021; Long et al. 2021). The seismogenic region is just located at the boundary between the Sichuan-Yunnan rhombic block and the southwest Yunnan block in

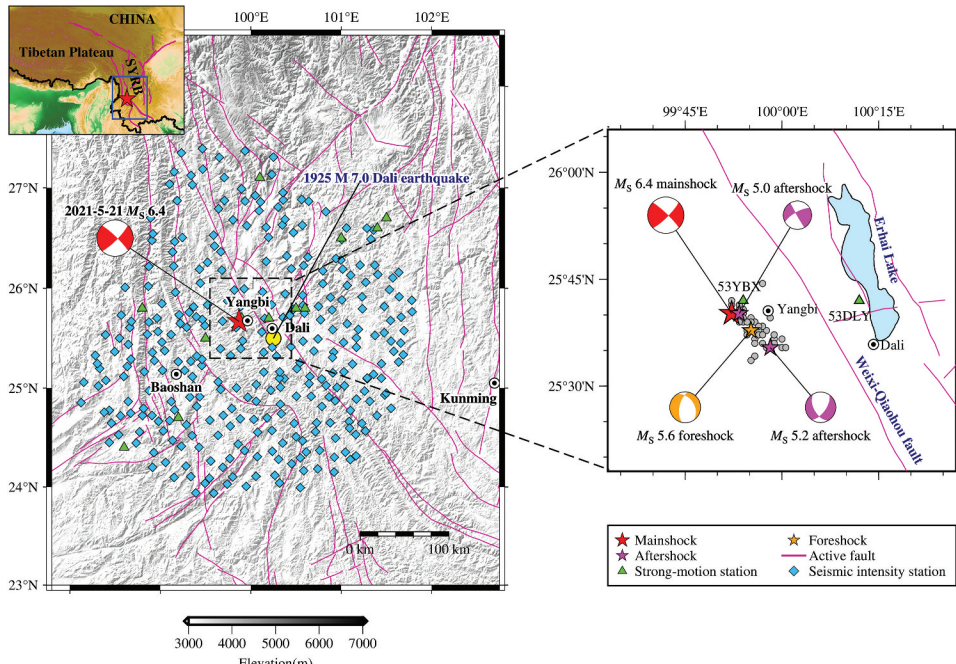


Figure 1. Epicenters of earthquakes with $M_S \geq 3.0$ in the 2021 Yangbi seismic sequence in southwest China. SYRB represents the Sichuan-Yunnan rhombic block on the southeastern margin of the Tibetan Plateau. Four events with $M_S \geq 5.0$ are highlighted by stars, while other events are plotted as dots. Triangles and squares represent the strong-motion and seismic intensity stations considered in this study, respectively. Blue solid lines represent the active faults, and the Weixi-Qiaohou fault is specially marked. Beach balls are plotted according to the focal mechanisms listed in Table 1.

Table 1. Basic information on the four earthquakes with $M_S \geq 5.0$ in the 2021 Yangbi seismic sequence.

Date (yyyy/mm/ dd)	Time (UTC +8, hh:mm: ss)	Latitude (°N)	Longitude (°E)	M_S	M_w	Focal depth (km)	Centroid depth (km)	First Nodal Plane (strike/ dip/rake) (°)	Second Nodal Plane (strike/dip/ rake) (°)	Number of recordings considered
2021/05/ 21	21:21:26	25.63	99.92	5.6	5.2	10	6.8	327/40/-127	192/59/-63	63
2021/05/ 21	21:48:34	25.67	99.87	6.4	6.1	8	6	45/80/7	314/83/170	325
2021/05/ 21	21:55:28	25.67	99.89	5.0	4.78	8	5	150/87/162	241/72/3	32
2021/05/ 21	22:31:10	25.59	99.97	5.2	5.1	8	9.2	150/53/-143	35/62/-44	130

The epicenter geographical coordinates, focal depth and surface wave magnitude (M_S) were derived from CENC; The focal mechanisms (M_w , strike, dip, rake) were derived from the global CMT catalog, except for the M_S 5.0 aftershock derived from Duan et al. (2021); The centroid depths of the four events are derived from Duan et al. (2021).

the southeast of Tibet Plateau (Xu et al. 2003) (Fig. 1). This region is one of the most seismically active regions in China for moderate-to-large earthquakes (Huangfu et al. 2007). The recorded historical earthquake with largest magnitude was the M 7.0 Dali earthquake in 1925 in this region (Ran and Wu 2019). Although few large earthquakes have struck this region over the past decades, the frequent occurrence of moderate events (e.g. the 2013 M_S 5.0 Eryuan earthquake, 2016 M_S 5.0 Yunlong earthquake, and 2017 M_S 5.1 Yangbi earthquake) also aroused special attention to the seismic hazard in this region.

Large numbers of strong-motion recordings (~2400) during this Yangbi sequence were obtained by the spatially sparse strong-motion stations in the National Strong Motion Observation Network System (NSMONS) of China and the spatially dense seismic intensity stations with an average interstation distance of 10–15 km in the national system for seismic intensity rapid reporting and earthquake early warning project of China. Totally, 12 strong-motion stations and 334 seismic intensity stations, which are not greater than 200 km from the epicenter of the M_S 6.4 mainshock, are in normal operation during this Yangbi sequence. More than one-third of the strong-motion data were collected from the four events with $M_S \geq 5.0$ (i.e. M_S 5.6 foreshock, M_S 6.4 mainshock, M_S 5.2 aftershock, and M_S 5.0 aftershock as listed in Table 1). The strong-motion stations are equipped with three-component force-balanced accelerometer sensors, 24-bit digitizers, and Global Positioning System timing. The seismic intensity stations are equipped with three-component Micro Electro-Mechanical System (MEMS) accelerometer sensors, 24-bit digitizers, and real-time digital signal transmission system (Peng et al. 2019). Peng et al. (2019) examined the performance of the MEMS sensors and confirmed the reliability of the accelerograms at seismic intensity stations. These strong-motion observation data furnish unique convenience for studying ground-motion characteristics in the southwest margin of the Sichuan-Yunnan rhombic block.

In this study, we aim to analyze the characteristics of strong ground motions obtained in the four $M_S \geq 5.0$ earthquakes in the Yangbi seismic sequence. We first provide an overall introduction of the strong-motion recordings, and introduce the waveforms obtained at near-source stations and the spatial distribution of peak amplitudes in the near-source areas. The source rupture directivity for the four earthquakes were investigated by fitting the azimuth-dependent residual terms with the rupture directivity function to explain the characteristics of waveforms and spatial distribution. We further compared the ground motion intensity measures with the predicted medians of ground motion prediction equations to reflect the source effects, and distance decay. Finally, we also compared the ground-motion durations with empirical models.

2. Overview of Strong-Motion Recordings

In this study, we assembled strong-motion recordings obtained at stations with epicentral distances (R_{epi}) not greater than 200 and 130 km for the M_S 6.4 mainshock and the other three events in the

Yangbi sequence, respectively, that is, 346 in M_S 6.4 mainshock, 166 in M_S 5.6 foreshock, 122 in M_S 5.0 aftershock, and 158 in M_S 5.2 aftershock. The strong-motion recordings at large epicentral distances were excluded due to the lower shaking amplitudes relative to the ambient noise. The overwhelming majority of these assembled recordings (~95%) were captured by the seismic intensity stations. In order to guarantee the quality of recordings, we reviewed the acceleration waveforms manually one by one for obvious problems (including missing one or two components, missing P wave, noisy recordings, extraordinary high or low-amplitude recordings, overlapping waveforms from two events, etc.), and eliminated these poor-quality ones. Finally, we retained 325, 63, 32, and 130 strong-motion recordings for the M_S 6.4 mainshock, M_S 5.6 foreshock, M_S 5.0 aftershock, and M_S 5.2 aftershock, respectively (Table 1). Figure 1 shows the geographical distribution of the strong-motion and seismic intensity stations which recorded the remaining data. Figure 2a plots the R_{epi} distribution of the remaining recordings from the four events in the Yangbi sequence. With the help of the dense seismic intensity stations around the epicentral area, a dozen near-field strong-motion recordings with $R_{\text{epi}} \leq 20$ km were well obtained, listed in Table 2. The strong-motion station 53YBX collected the recording with the minimum R_{epi} (i.e. 3.48 km) from the M_S 5.0 aftershock.

The remaining recordings were processed following the procedure as done by Wang and Wen (2021). The baseline correction is first performed for subtracting the mean from the entire waveform. Then, cosine tapers with a width of 2.0 s are added near the beginning and end of the waveform by searching for the first and last zero crossings to avoid truncation effects, and zero

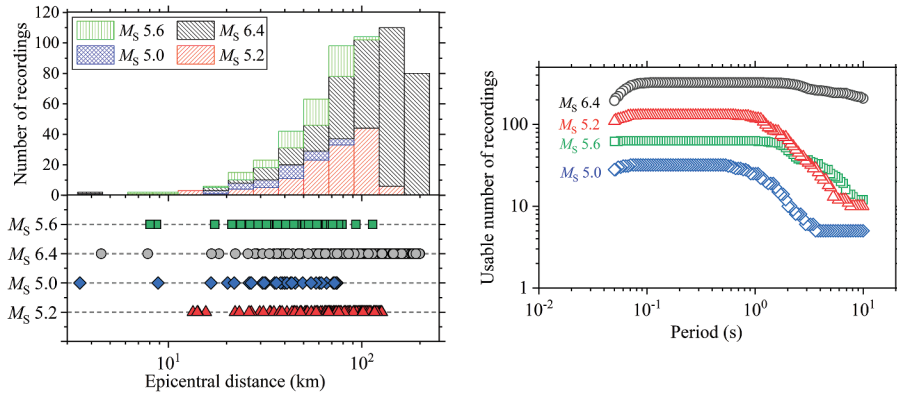


Figure 2. (a) The epicentral distance (R_{epi}) distribution of the recordings considered from the four earthquakes in the Yangbi sequence. (b) the number of usable horizontal PSAs versus period.

Table 2. Near-field strong-motion recordings with $R_{\text{epi}} \leq 20$ km from the four $M_S \geq 5.0$ earthquakes of Yangbi sequence.

Event	Station	Latitude (°N)	Longitude (°E)	R_{epi} (km)	R_{rup} (km)	PGA (cm/s ²)			PGV (cm/s)		
						EW	NS	UD	EW	NS	UD
M_S 5.6 foreshock	53YBX	25.70	99.90	8.04	12.83	328.94	265.40	190.75	21.63	9.14	5.44
	L2203	25.61	99.84	8.68	13.24	79.18	104.06	52.53	3.90	3.53	1.88
	L2205	25.47	99.91	17.37	20.00	61.01	60.60	32.76	1.88	2.73	1.02
M_S 6.4 mainshock	53YBX	25.70	99.90	4.49	2.24	347.55	695.24	409.21	35.05	32.21	7.24
	L2203	25.61	99.84	7.82	10.88	190.94	292.83	184.43	12.80	13.07	4.63
	L2204	25.82	99.89	16.70	14.68	155.28	166.67	90.51	5.13	7.57	2.78
M_S 5.0 aftershock	L2201	25.67	99.69	18.24	15.42	64.71	70.15	49.71	3.42	3.34	1.85
	53YBX	25.70	99.90	3.48	8.73	123.85	117.98	63.86	3.78	3.87	1.84
	L2203	25.61	99.84	8.84	11.92	18.33	32.55	12.64	0.79	0.92	0.48
M_S 5.2 aftershock	L2204	25.82	99.89	16.60	18.43	33.04	20.24	12.05	0.60	0.57	0.26
	53YBX	25.70	99.90	14.10	15.60	130.69	177.04	81.68	7.80	5.06	3.04
	L2203	25.61	99.84	13.39	16.21	39.42	32.38	28.97	1.27	1.70	0.82
	L2205	25.47	99.91	14.20	16.30	72.59	123.59	38.52	2.63	4.75	1.46
	L0102	25.56	100.12	15.60	17.53	151.27	95.10	61.78	2.33	1.19	1.25

pads with a length dependent on the high-pass corner frequency (f_{hp}) and filter order are further added to the beginning and end to remove the spurious low-frequency noise (Boore 2005). Finally, an acausal four-order Butterworth band-pass filter is applied in the time domain. The high-pass and low-pass corner frequencies (f_{lp}) for each component are determined by the signal-to-noise ratios (SNRs) according to a threshold of 3.0. The well-processed strong-motion accelerograms are then integrated to obtain velocity and displacement waveforms. The peak amplitudes, including peak ground acceleration (PGA), and velocity (PGV) were obtained at three components (i.e. east-west, north-south, and up-down components). The horizontal PGA and PGV are represented by the RotD50 measures independent of instrument orientation (Boore 2010). The horizontal 5%-damped pseudospectral accelerations (PSAs) also represented by RotD50 measures are computed at 200 log-spaced periods from 0.05 to 10 s. The low and high boundaries for the usable period range of PSA were defined by $f_{lp}/1.25$ and $1.25f_{hp}$, respectively (Abrahamson and Silva 1997). Figure 2b plots the number of usable horizontal PSAs versus period, and the number sharply decreases with periods greater than ~ 1.0 s. In order to illustrate the determination of f_{lp} and f_{hp} , Fig. 3 provides two typical examples, one with high SNRs at all period ranges, and the other with high SNRs at partial period range. The f_{lp} and f_{hp} are both ends of a period range where SNRs are always greater than a threshold of 3.0. Figure 3 also highlights the extracted S-wave and pre-P-noise windows with the same length, and the corresponding Fourier amplitude spectra at a frequency range of 0.08–25 Hz smoothed using the Konno-Ohmachi window (Konno and Ohmachi 1998) for calculating SNRs. Figure 4a compares the accelerograms and PSAs recorded at the strong-motion station 53DLY and the seismic intensity station L0101 in the mainshock. The interstation distance between both stations is just 4.57 km. The waveforms and intensities of ground shakings recorded by both stations did

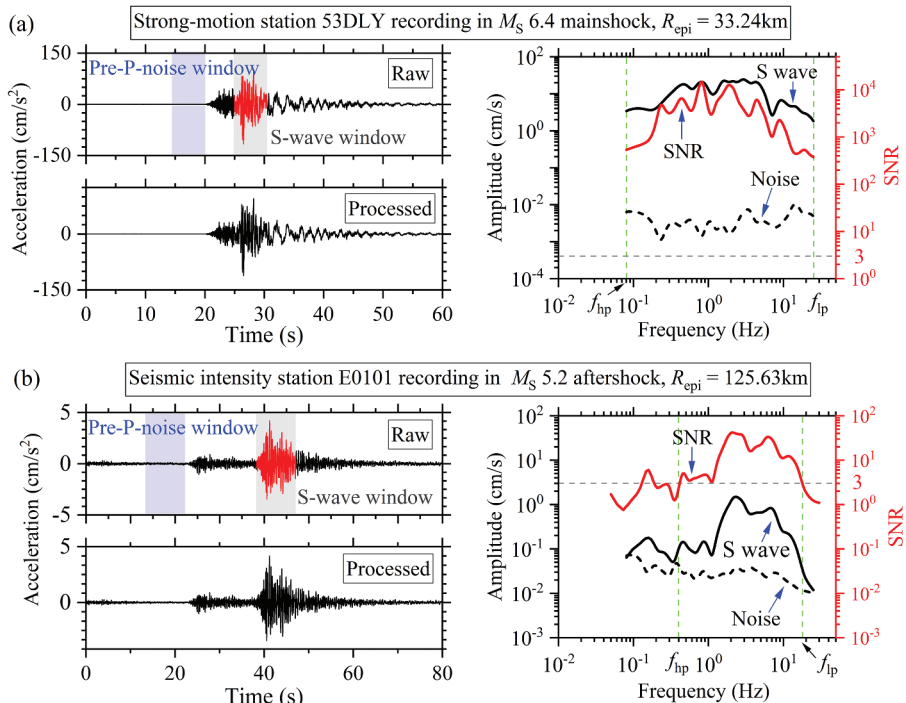


Figure 3. Two examples for illustrating the determination of low-pass (f_{lp}) and high-pass (f_{hp}) corner frequencies. The S-wave and pre-P-noise windows with the same length were extracted, and their Fourier amplitude spectra were calculated and smoothed for further retrieving SNRs. The f_{lp} and f_{hp} are identified as both ends of a period range where SNRs are always greater than a threshold of 3.0.

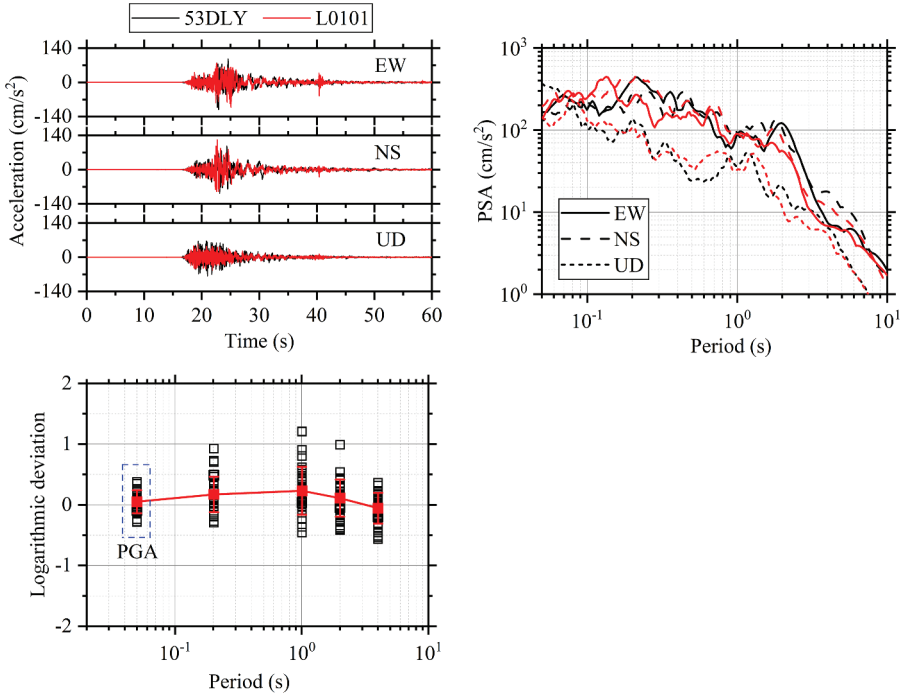


Figure 4. (a) The motion-to-motion comparisons for recordings obtained from close-by stations in both observation networks. (b) the logarithmic deviations of PGAs and PSAs at periods of 0.2, 1.0, 2.0 and 4.0 s for the 12 strong-motion stations triggered by the M_S 6.4 mainshock and their corresponding neighboring intensity-network stations.

not show any obvious discrepancies. Furthermore, we compared the PGAs and PSAs at the 12 strong-motion stations and their nearby seismic intensity stations in the mainshock. The logarithmic deviations of the PGAs and PSAs at the strong-motion stations to those at the seismic intensity stations were shown in (Fig. 4b). The small deviations at the majority of close-by stations indicate the approximately coincident observations from both networks.

Figure 5 plots the acceleration, velocity, and displacement waveforms captured by station 53YBX from the four earthquakes in the Yangbi sequence. The station is 8.04, 4.49, 3.48, and 14.10 km away from the epicenters of the M_S 5.6 foreshock, M_S 6.4 mainshock, M_S 5.0, and M_S 5.2 aftershocks, respectively. The ground shakings lasted for a short time, ~8 s for the mainshock, and ~5 s or less for the other three events. Except for the recordings at up-down component from both aftershocks, the PGAs are all greater than 100 cm/s², valuable for the seismic design of engineering structures. The PGA at north-south component of recording from the M_S 6.4 mainshock reaches a maximum of 695.24 cm/s². We also noted that one-sided displacement and two-sided velocity pulses clearly appear in the mainshock recording, more or less in recordings from the other three events. The method proposed by Shahi and Baker (2014) was then applied to identify the velocity pulse-like waveforms from the near-field recordings with $R_{\text{epi}} \leq 20$ km (not limited to the four obtained at 53YBX station, see Table 2). In the identification algorithm, the continuous wavelet transforms were performed with the fourth Daubechies wavelet as the mother wavelet to decomposes the velocity signals into shapes localized in small time and frequency bands. The continuous wavelet transform of the velocity time history is computed, and the coefficient with the largest absolute value is identified. The wavelet associated with this coefficient identifies the period and position of the pulse. The mainshock horizontal-component recordings at station 53YBX only were characterized by the obvious velocity pulse-like waveforms according to the Shahi-Baker identification criteria, suggesting the potential

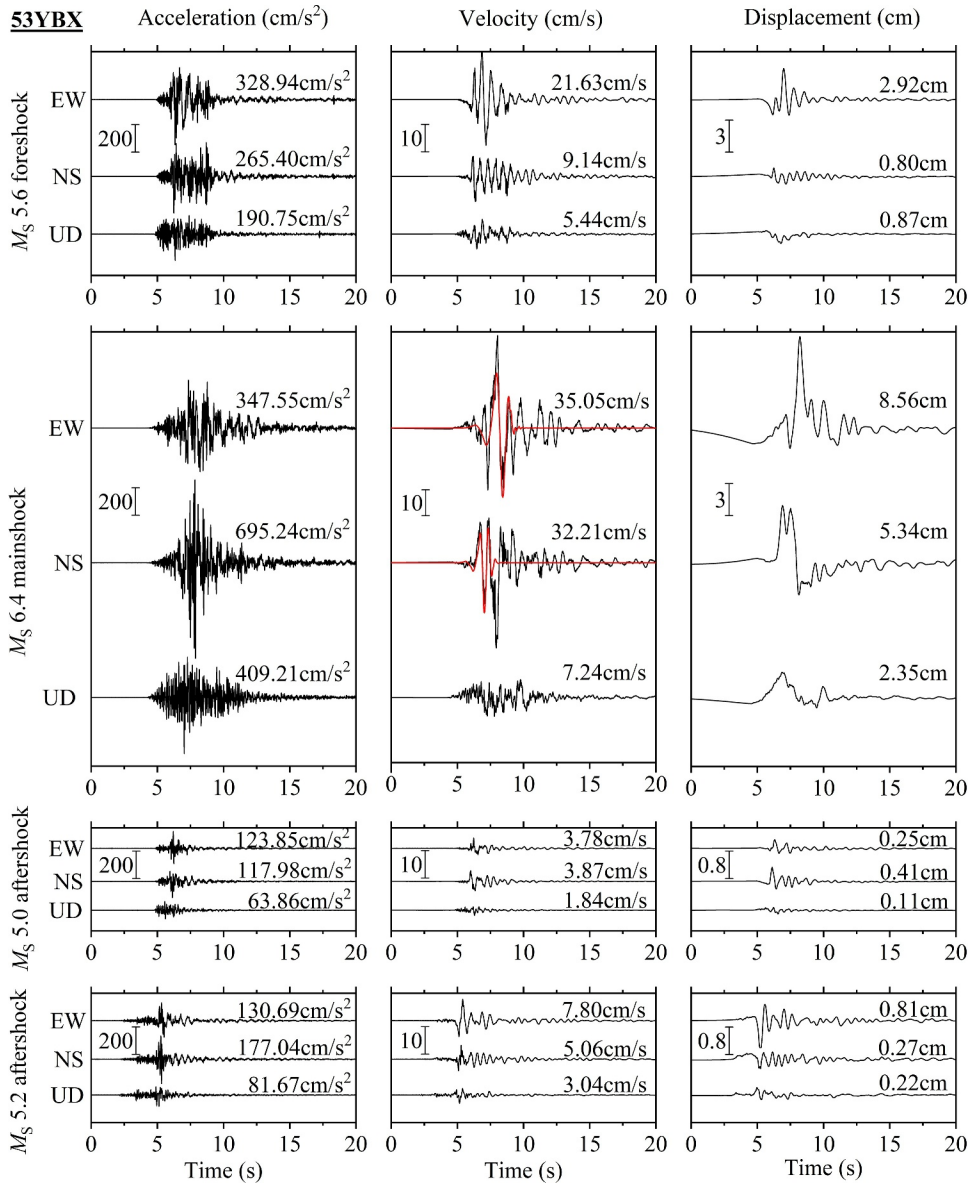


Figure 5. The acceleration, velocity, and displacement waveforms at east-west (EW), north-south (NS), and up-down (UD) components were captured by station 53YBX during the four earthquakes with $M_S \geq 5.0$ in the Yangbi sequence. The peak ground accelerations (PGAs), velocities (PGVs), and displacements (PGDs) are labeled on each panel. The red lines indicate the extracted long-period velocity pulses.

rupture directivity in this event. The long-period velocity pulses were extracted using the wavelet transform algorithm and plotted in Fig. 5. Although we caught sight of the velocity pulse-like features from some near-field recordings, they can not be identified as velocity pulse-like waveforms due to the low amplitudes with PGV not greater than 30 cm/s, which hardly cause potential damage for well-designed buildings.

Figure 6 provides an overall description of the spatial variability of ground motions around the epicentral area in the $M_S 6.4$ mainshock. The peak amplitudes (PGAs, and PGVs) at both horizontal and up-down components are respectively interpolated according to the minimum-curvature tension

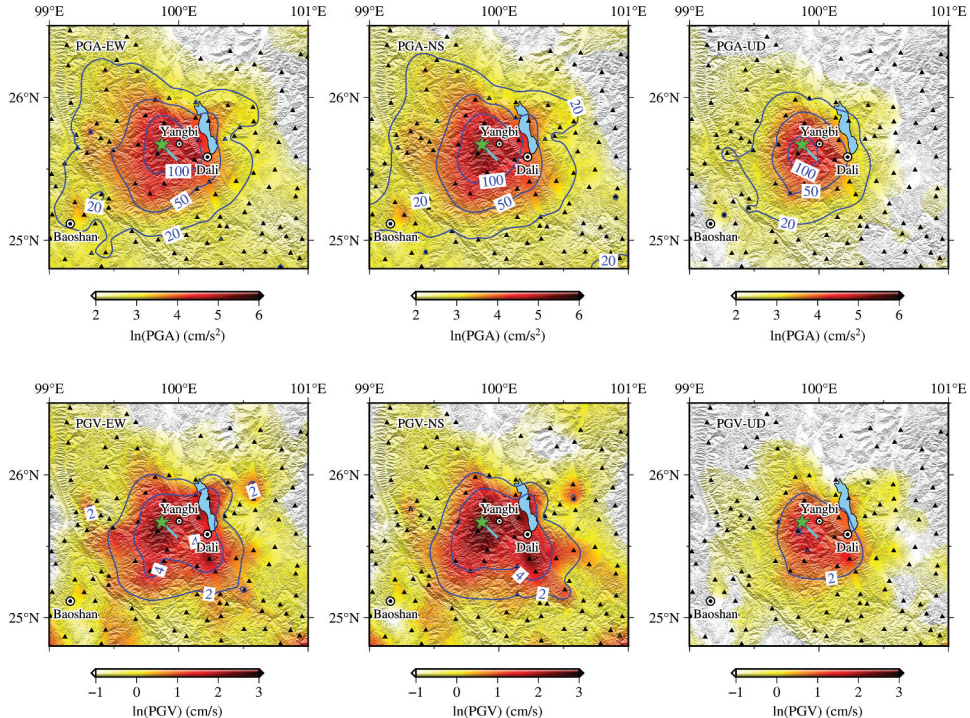


Figure 6. Spatial variability of ground motions in the M_S 6.4 mainshock. The horizontal and vertical peak amplitudes (PGAs and PGVs) are interpolated. Star indicates the earthquake epicenter. The cyan rectangle indicates the surface projection of the rupture fault inverted by (Yang, Wen, and Xu 2021).

gridding algorithms (Smith and Wessel 1990). The strongest ground shakings mainly concentrate around the surface projection of the rupture fault derived from the kinematic inversion of source rupture of Yang, Wen, and Xu (2021). The PGA and PGV contours elongated approximately in both northwest-southeast (in consistency with the trending of fault plane) and northeast-southwest (perpendicular to the trending of fault plane) directions. The stronger ground motion is distributed in an elongated pattern along the northwest-southeast direction centered on the axis of the fault. The spatial extension also predominant in the northeast-southwest direction is more obvious for the horizontal PGA and PGV contours than the vertical ones. This pattern may be attributed to local site effects amplification caused by the low-velocity sedimentary layers around the Erhai Lake in the northeast and Baoshan city in the southwest. It was also noted that peak amplitudes, in particular PGVs, show the asymmetric attenuation with the source-to-site distance that is much slower distance decay toward the southeast. We preliminary inferred that it may be ascribed to the source rupture directivity, always resulting in the spatially asymmetric ground motions.

3. Rupture Directivity

The spatial distribution and the velocity pulse-like waveforms in the M_S 6.4 mainshock prompt us to expect the potential source rupture directivity (either the unilateral or the asymmetrical bilateral rupture propagation). In this study, the rupture directivity patterns for the four earthquakes in Yangbi sequence were estimated by fitting directivity functions, universally used in large numbers of previous studies (e.g. Boatwright 2007; Kane et al. 2013). The ground motion prediction equation (GMPE) describes the ground motion intensity measures (e.g. PGA, PGV, and PSA) varied with source-dependent factors (e.g. magnitude, fault type, focal depth), source-to-site distance, near-surface

geology condition, and others. However, the rupture directivity effects, usually leading to significant azimuthal dependence in ground motion durations and amplitudes are generally not covered by GMPE. Therefore, the directivity effects in ground-motion recordings are inferred by analyzing the azimuthal dependence in residual terms corrected for systematic contributions related to the source, propagation, and site (e.g. Ren, Wang, and Wen 2017; Sgobba, Lanzano, and Pacor 2021). The rupture directivity effects are usually expressed in the simple form of C_d^γ . After eliminating the rupture directivity effects from the observed ground motions, the corrected residual terms will theoretically achieve a minimum. The following equation was thus used to obtain the optimum C_d , i.e.

$$\sum_{i=1}^N [\log_{10}(Y_i^O/C_d^\gamma) - \log_{10}(Y_i^P)]^2 = \min., \quad (1)$$

where Y_i^O and Y_i^P represent the observed and predicted ground motions, respectively, and N is the number of the ground motion recordings.

Under the assumption of a homogeneous kinematic linear source model, the rupture directivity coefficient C_d was originally proposed by Ben-Menahem (1961) for unilateral rupture and improved by Boatwright (2007) for asymmetrical bilateral rupture, which was expressed as,

$$C_d = \sqrt{\frac{k^2}{\left[1 - \left(\frac{v_r}{\beta}\right)\cos\vartheta\right]^2} + \frac{(1-k)^2}{\left[1 + \left(\frac{v_r}{\beta}\right)\cos\vartheta\right]^2}}, \quad (2)$$

where v_r/β is the Mach number (v_r is the rupture velocity and β is the shear-wave velocity). The parameter ϑ is the angle between the ray that leaves the source and the direction of rupture propagation (Joyner 1991), which can be expressed simply as the difference between the horizontal rupture direction φ and the source-to-site azimuth. The parameter k represents the relative portion of rupture length in the rupture direction φ accounting for the entire rupture length. The exponent γ is dependent on the source model considered. In this study, $\gamma = 1.0$ was used (Wen, Wang, and Ren 2015).

In this study, the horizontal PGAs (i.e. the geometrical mean for both horizontal components) were used for the estimation of source rupture directivity for the four earthquakes in Yangbi sequence. The GMPE developed by Yu, Li, and Xiao (2013; hereinafter Yu13) for the Tibetan region was used to compute the predicted PGAs at rock sites. The Yu13 model was constructed by the macroseismic intensity projection method and used for mapping seismic hazard in China. In order to eliminate the effect of the fault trending included in the Yu13 model, the PGA predictions were first calculated using a series of fault trending from 0° to 180° at an interval of 0.1° , and their average was then used as the prediction. The PGA amplification coefficients for various site classes specified in the Chinese code for seismic design of buildings were further used to consider the local site effects (Gao 2015). The site classes were classified into different categories according to the empirical relationship between V_{S30} (i.e. the time-weighted average shear-wave velocity over the upper 30 m) values and the site classification, that is, >510 m/s for class-I site, 260–510 m/s for class-II site, 150–260 m/s for class-III site, and <150 m/s for class-IV site (Lyu and Zhao 2007). Due to the unavailable borehole velocity profile at stations in this study, their V_{S30} values were derived from the slope-based estimations (Heath et al. 2020). The V_{S30} values at stations are mainly in the range of 181.95–900.0 m/s, corresponding to class-I, -II, and -III sites.

In order to eliminate the overall misfit of the specific source to the mean source term in GMPE, and the potential differences in far-field anelastic attenuation, the path-corrected intra-event residuals were used to estimate the source rupture directivity, as shown in Fig. 7. The significant azimuthal dependence occurs in the residuals in the M_S 6.4 mainshock. We also found azimuth-dependent residuals for the M_S 5.6 foreshock more or less. However, no azimuthal dependence in residuals was observed for both aftershocks.

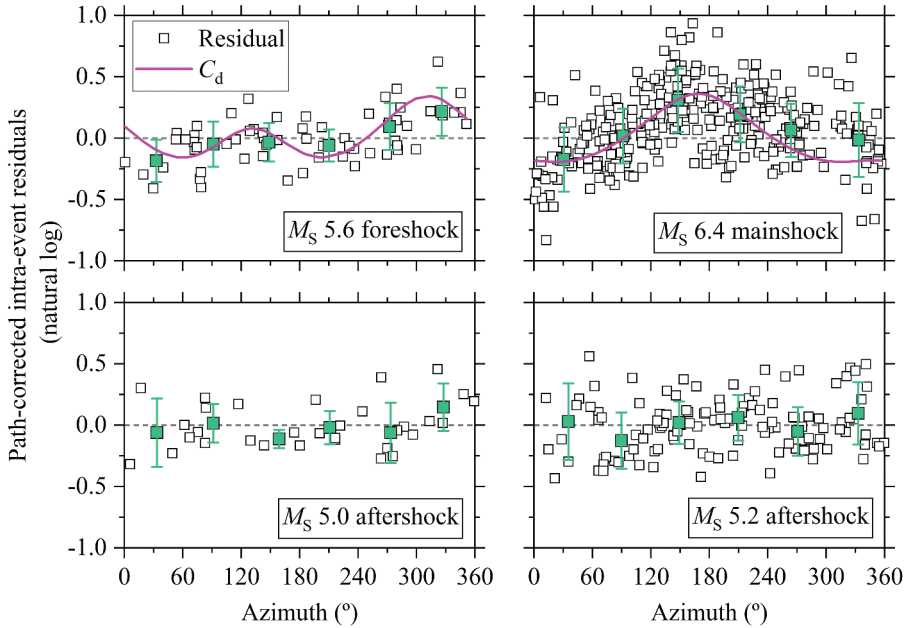


Figure 7. Path-corrected intra-event residuals for PGAs against azimuths for the four events in the Yangbi sequence. The azimuth-binned means are represented by the blue squares with bars indicating one standard deviation. The directivity function $\log_{10}(C_d)$ was used to fit the azimuth-dependent residuals.

We used a grid-searching technique to obtain the optimum rupture directivity parameters (including φ , v_r/β and k) for the M_S 5.6 foreshock and the M_S 6.4 mainshock, and the best-fitted C_d curves were also plotted in Fig. 7. The M_S 6.4 mainshock shows the asymmetric bilateral rupture with approximately 85% of rupture propagating ($k = 0.85$) toward the south-southeast direction ($\varphi = 165.9^\circ$) with $v_r/\beta = 0.63$. The aftershocks relocations also revealed the potential NNW-SSE trending fault (Duan et al. 2021; Long et al. 2021). The coseismic slip inversion also revealed the approximately unilateral rupture propagation in the SSE direction (Yang, Wen, and Xu 2021). Its rupture velocity is about 2.24 km/s according to the shear-wave velocity of 3.55 km/s in the CRUST 1.0 model (Laske et al. 2013), which is consistent with the rupture velocity of 2.2 km/s provided by Chen et al. (2022) and Gong et al. (2021). The M_S 5.6 foreshock ruptured the approximately NW-SE trending fault, and the predominant rupture propagation is approximately in the NW direction ($k = 0.66$, and $\varphi = 311.6^\circ$) with $v_r/\beta = 0.70$.

As the large-scale construction and operation of the dense seismic intensity stations in China, the ground-motion data in real-time transmission will provide a good chance for rapid estimation of source rupture directivity by fitting the rupture directivity function. The rapid estimation of rupture directivity will play an important role in the seismic intensity rapid and reliable reporting.

4. Comparisons with GMPEs

Up to now, GMPEs for predicting PSAs for earthquakes in Yunnan Province have not been developed based on the strong-motion data according to a general review of GMPEs (Douglas 2021), although the ground-motion recordings from the 2014 M_S 6.5 Ludian earthquake and the 2014 M_S 6.6 Jinggu earthquake in Yunnan Province have been adopted for the development of a GMPE applicable for Sichuan-Yunnan region by Li et al. (2020). In order to reveal the source effects and distance decay, the horizontal PGAs, and PSAs recorded in the four earthquakes of Yangbi sequence were compared with the predicted medians of GMPEs developed by Abrahamson, Silva, and Kamai (2014; hereinafter



ASK14) and Chiou and Youngs (2014; hereinafter CY14) for global shallow crustal earthquakes in active tectonic regions based on the NGA-West2 database. The rupture distance (R_{rup} ; the shortest distance to the rupture fault) is used as distance measure in both ASK14 and CY14 models. The R_{rup} values for recordings in the M_S 6.4 mainshock were calculated according to the rupture fault geometry provided by Yang, Wen, and Xu (2021), as shown in Fig. 1. However, in view of the unavailable rupture fault for other earthquakes considered, the hypocentral distance approximately substitutes for the R_{rup} . The Z_{TOR} (the vertical distance to the shallowest point on the rupture) is used in both ASK14 and CY14 GMPEs to account for the effects of the buried depth of the strong motion generation area, which is defined by the rupture fault for the M_S 6.4 mainshock ($Z_{\text{TOR}} = 1.753$ km) or as the centroid depth for other earthquakes (Table 1). The aftershock scaling, and basin term were not considered for computing the predicted medians. The regional adjustment of anelastic attenuation for China was applied. The V_{S30} dependence of site amplification was included. The strike-slip fault type for M_S 6.4 mainshock and M_S 5.0 aftershock, and the normal fault type for M_S 5.6 foreshock and M_S 5.2 aftershock were specified by the plunges of pressure and tension axes from the global CMT catalog. The predicted medians for PGA, and PSAs were computed for the four earthquakes in Yangbi sequence.

We first computed the total residuals (R_{es}) between the observed PGAs and PSAs and the predicted medians by the ASK14 and CY14 models, as shown in Fig. 8. According to the negative residuals in general, both models provide the systematic overpredictions relative to the observed values from the four earthquakes of Yangbi sequence, which is practically equivalent to a negative event term. To classify the roles of source, propagation path, and local site in ground motions, the residual analysis was performed, and the total residual was then divided into the inter-events residual (δB_e) and the intra-event residual (δW_{es}), as proposed by Al Atik et al. (2010). The δB_e represents the average deviation of ground motions observed from an earthquake with respect to the mean of the predicted medians by a GMPE. The δW_{es} is the difference between the observed value at an individual station and the specific-earthquake predicted median.

The δB_e values for the four earthquakes in Yangbi sequence were plotted in Fig. 9, as well as the inter-events standard deviation (shaded area) describing the event-to-event scatter in the ASK14 and CY14 models. The negative δB_e values at all periods (0.05–5.0 s) indicate the relatively weaker source contributions to ground motions in the Yangbi sequence compared with the mean source contributions from the global shallow crustal earthquakes represented by both the ASK14 and CY14 models. Generally, the negative δB_e values in most periods are not within the range of one inter-event standard deviation of both GMPE models. For the mainshock, the δB_e values from the ASK14 model are significantly greater than those from the CY14 model at $T > 0.2$ s, indicating that underprediction of the source term on intermediate- and long-period provided by the ASK14 model. For the foreshock and aftershocks, the δB_e values from the ASK14 model are slightly lower than from the CY14 model at $T < 0.2$ s, indicating relatively underprediction of the source contribution for short periods provided by the CY14 model. The δB_e values approximately share the similar level for the M_S 5.6 foreshock, the M_S 6.4 mainshock, and the M_S 5.2 aftershock, and no apparent trends with period occur. It was also noted that the δB_e values at short periods (< 0.3 s) in the three events appear to be varied, steadily ranking from high to low in order of the M_S 5.6 foreshock, the M_S 6.4 mainshock, and the M_S 5.2 aftershock. Since δB_e is the event-specific deviation from the predicted median for the population, the variability in those source parameters contributing to the ground motion but not modelled by the GMPE (e.g. the stress drop) is expected to affect the between-event distribution. The inter-event residuals (δB_e) for the observed and predicted median of GMPEs show a clear dependence on the Brune's stress drop, as pointed out in previous studies (Ameri et al. 2017; Bindi et al. 2007; Bindi, Spallarossa, and Pacor 2017). This characteristic reveals the earthquake type-dependent source contributions on short-period ground motions, gradually weakening in order of foreshock, mainshock, and aftershock, which may be related to the dependence of stress drop on earthquake type. A large number of studies have generally found the much smaller stress drops for aftershocks in comparison with the mainshock in the mainshock-aftershock sequence (e.g. Baltay, Hanks, and Abrahamson 2019;

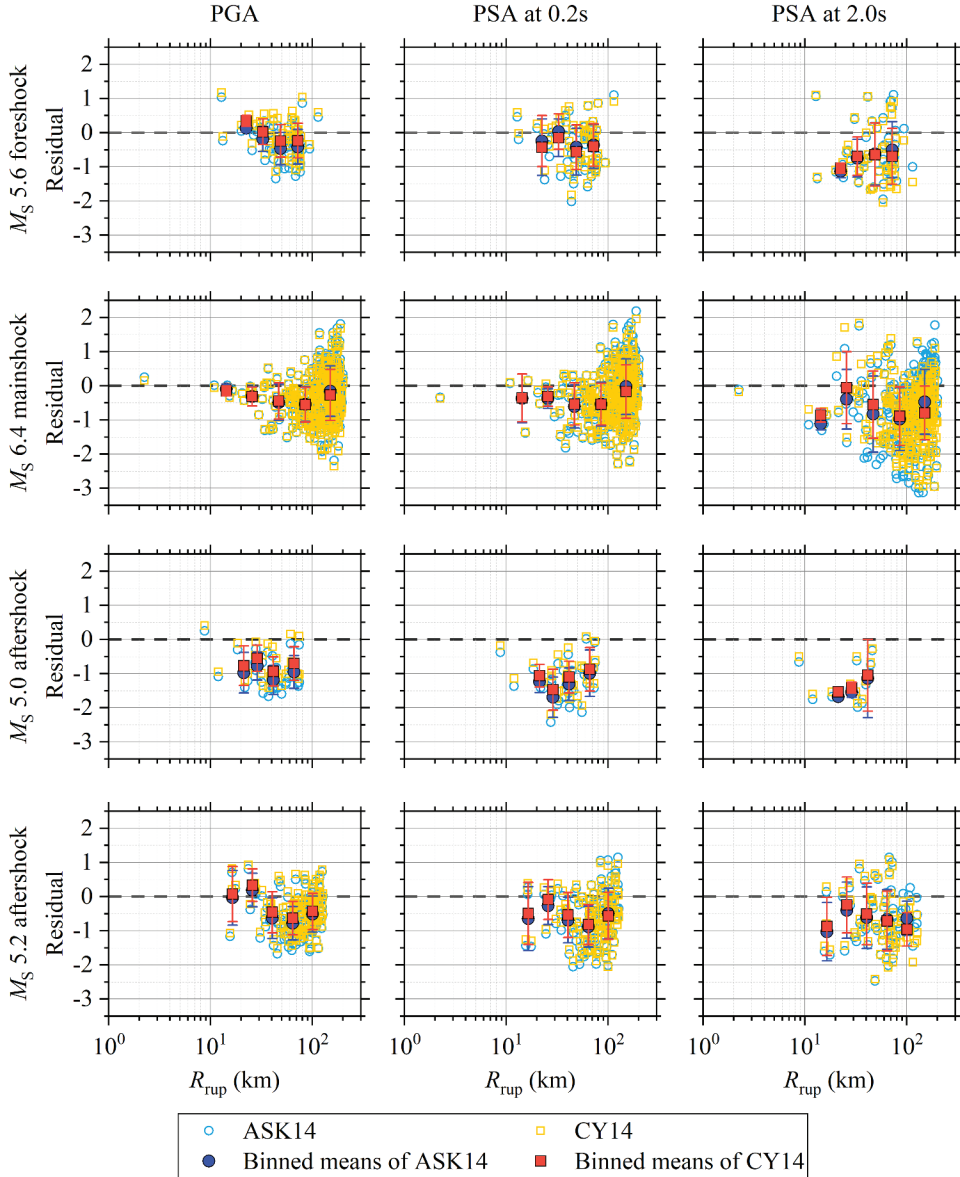


Figure 8. Total residuals (R_{es}) between the observed values and the predicted medians by the ASK14 and CY14 models for PGA, PGV and PSAs for periods 0.2, and 2.0 s for the four $M_s \geq 5.0$ earthquakes in the 2021 Yangbi sequence.

Moyer et al. 2018; Trugman and Shearer 2018). Particularly, the M_s 5.0 aftershock displays the most negative δB_e values, far below the general level in the other three events, indicating its weakest source contributions to ground motions. The δB_e values for the M_s 5.2 aftershock are also much higher than those for the M_s 5.0 aftershock. The M_s 5.0 aftershock immediately follows and is in close proximity to the M_s 6.4 mainshock, while the M_s 5.2 aftershock is farther from the mainshock. The very different source contributions between both aftershocks may be ascribed to the distance to the mainshock. For example, Baltay, Hanks, and Abrahamson (2019) found the smaller stress drops for those aftershocks close to the mainshock fault. We inferred that the M_s 5.0 aftershock is more likely to rupture the highly damaged or fractured area by the previous mainshock, and thus exerts the very weak source contributions on ground motions. From this point, an aftershock term related to the factors describing

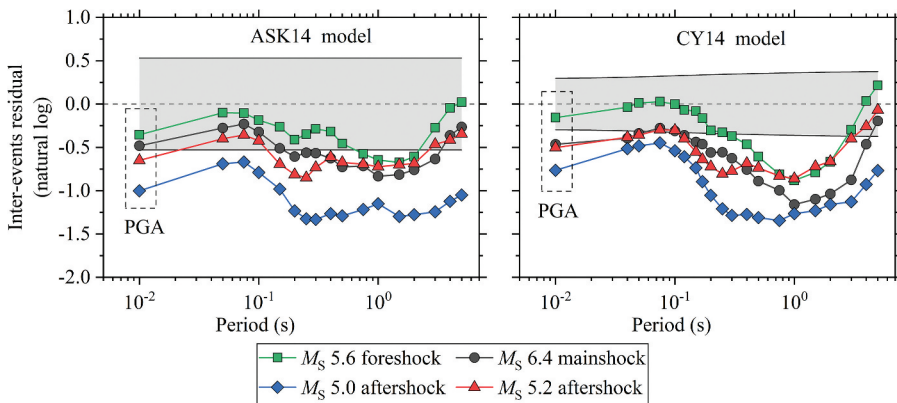


Figure 9. Inter-events residual (δB_e) for PGA and PSAs at periods of 0.05–5.0 s for the four earthquakes in Yangbi sequence based on the ASK14 and CY14 models. The shaded area indicates the inter-events standard deviation describing the event-to-event scatter in the both models.

the spatial and temporal distance between aftershock and mainshock may be helpful for the accurate estimation of ground motions.

The δW_{es} values were further calculated by subtracting δB_e from the total residuals based on the ASK14 and CY14 models, respectively. Figure 10a plots the δW_{es} values for PGA, and PSAs at periods of 0.2, 2.0, and 4.0 s in the four earthquakes of Yangbi sequence. The δW_{es} mean and standard deviation at each distance bin from 10 to 200 km at a width of 0.1 in log units were calculated and also plotted in Fig. 10a. The upward trends clearly occur as the distance increases at large distances (>100 km), clearly indicating the weaker anelastic attenuation in this study region. In order to quantitatively describe the difference of anelastic attenuation in the study region from that represented by the ASK14 and CY14 models, the values of adjustment coefficient Δc_3 were obtained from the linear regression between δW_{es} and R_{rup} according to the linear form of $\delta W_{es} = \Delta c_3 (R_{rup} - R_{ref}) + \delta W_{IR}$ for PGA and PSAs at periods from 0.05 to 5.0 s based on the recordings with $R_{rup} \geq 15$ km, as shown in Fig. 10a. In the linear form, the reference distance R_{ref} is fixed to 1.0 km, and δW_{IR} is approximately the mean of δW_{es} values at close distances. The almost positive Δc_3 values account for the weaker anelastic attenuation (high Q) in the study region compared with other active tectonic regions from both GMPEs (see Fig. 10b). We also compared the Δc_3 values in this study with those derived for the Lushan and Jiuzhaigou earthquakes in the Sichuan region (Ren et al. 2018). The values of Δc_3 in this study are somewhere between those positive ones derived for the Lushan and Jiuzhaigou events. The results show that anelastic attenuation is generally lower in a wide region of Yunnan-Sichuan than the global shallow crustal earthquakes in active tectonic regions that considered by the ASK14 and CY14 prediction models.

5. Ground-Motion Duration

The ground-motion duration is also a fundamental parameter to characterize the ground shaking. The significant duration, the most commonly used duration metric in engineering applications is defined from the time elapsed between various percentages of Arias intensity (Trifunac and Brady 1975). Our study considered the 5%-95% significant durations (D_{5-95}) for ground-motion recordings at both horizontal components in the four earthquakes of Yangbi sequence. To avoid the instability due to the early and late times at which the 5% and 95% levels are reached, respectively, the D_{5-95} is approximately represented by 20%-80% significant duration (D_{20-80}) multiplied by a scale factor of 2.0 (Boore and Thompson 2014) this is, $D_{5-95} = 2 \times D_{20-80}$. The D_{5-95} geometrical means at both horizontal components were shown in Fig. 11a. The predicted medians by the GMPE proposed by Afshari and

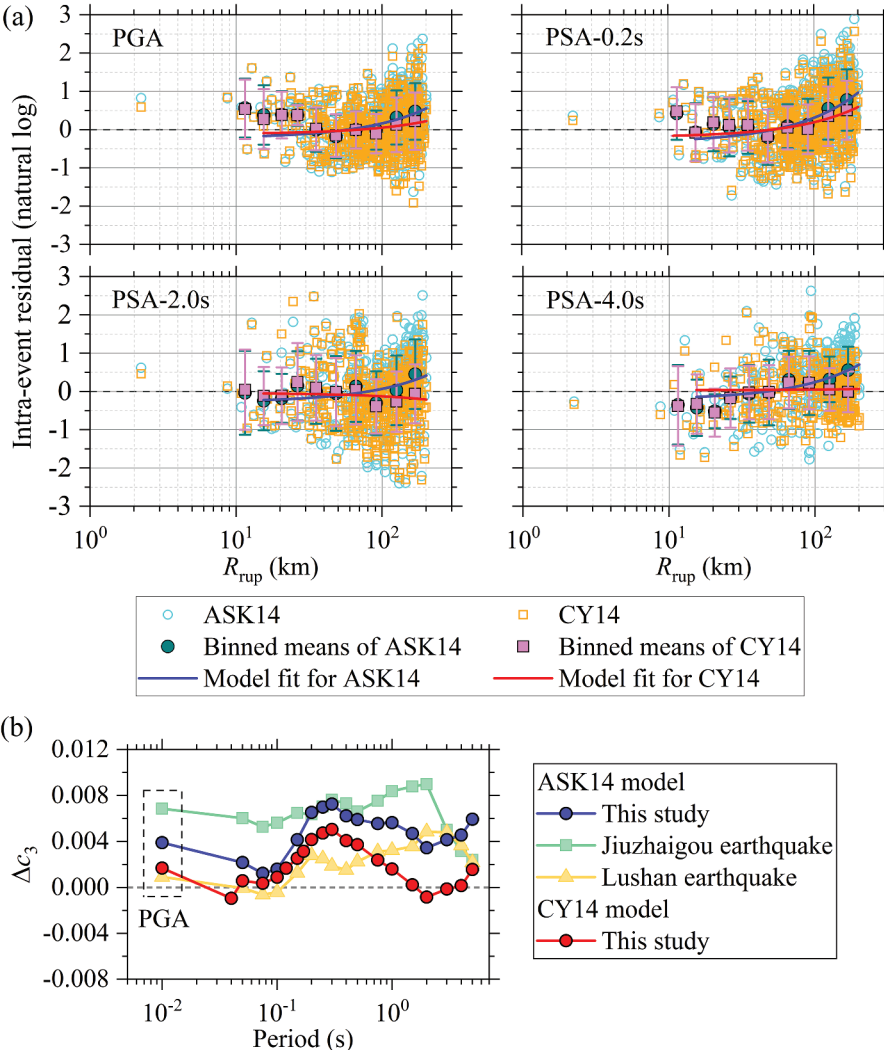


Figure 10. (a) Intra-event residuals (δW_{es}) for PGA and PSAs at periods of 0.2, 2.0, and 4.0 s against R_{rup} for the four earthquakes of Yangbi sequence based on the ASK14 and CY14 models. Distance-binned means (squares) with one standard deviation (error bars) are plotted. The trend lines of δW_{es} against R_{rup} were obtained from the linear regression based on data with $R_{\text{rup}} > 15$ km. (b) Values of adjustment coefficient ΔC_3 derived from the linear regression between δW_{es} and R_{jb} for PGA and PSAs at periods of 0.05–5.0 s. We also compared the ΔC_3 values for the Lushan and Jiuzhaigou earthquakes (Ren et al. 2018).

Stewart (2016; hereinafter AS16) for shallow crustal earthquakes in active tectonic regions were calculated and plotted in Fig. 11a for comparisons. The predicted values were separately estimated at each station adopting the source-, path-, and site-related parameters. The predicted medians are overall in good agreement with the observed values in the four earthquakes. The distance scaling of D_{5-95} can be well described by the AS16 model. Figure 11a also depicts the empirical model of path duration (D_p) developed for active tectonic regions by Boore and Thompson (2014; hereinafter BT14). The ground-motion duration consists of the distance-dependent path duration and the source duration relating to the size of source rupture. The BT14 model well describes the distance scaling of ground-motion duration, although the BT14 model overall is lower than ground-motion durations in the M_S 6.4 mainshock (a large event with longer source duration).

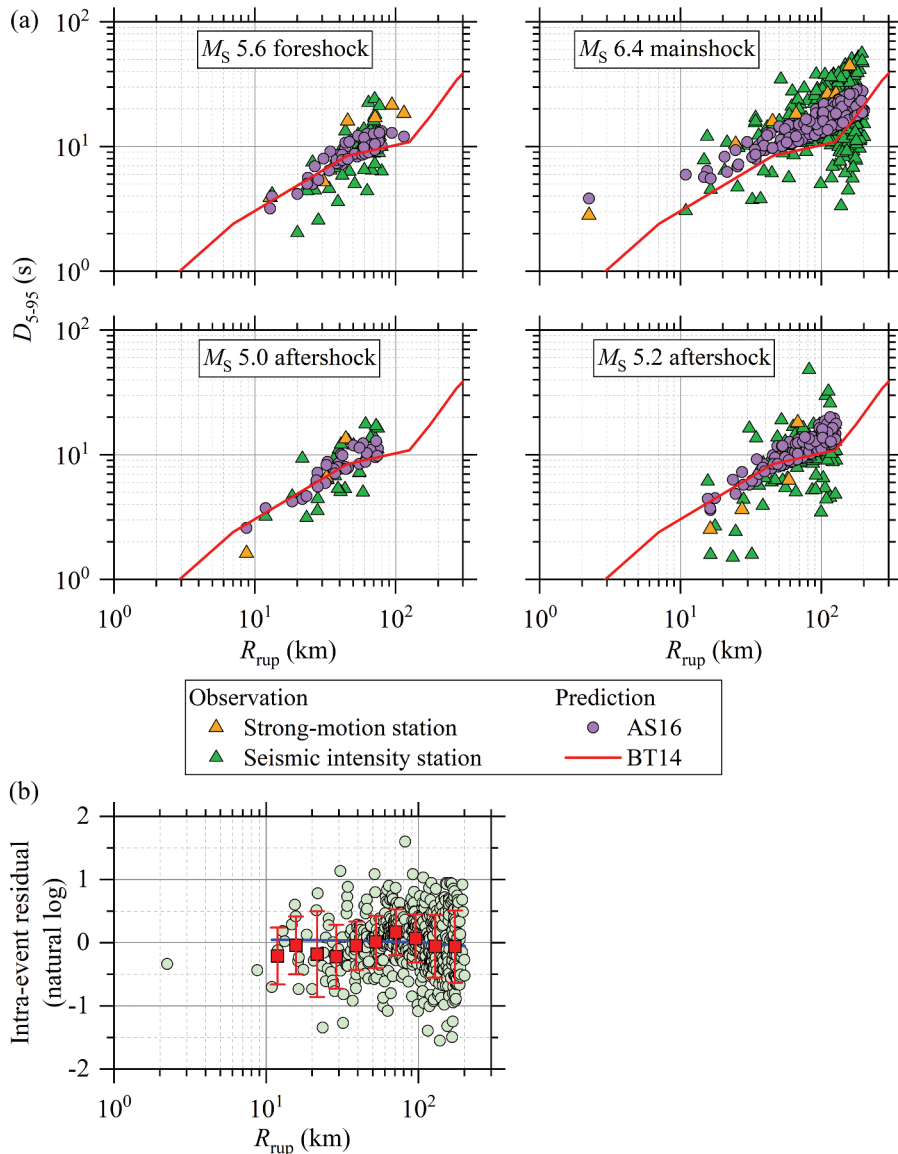


Figure 11. (a) Comparison of 5%-95% significant durations (D_{5-95}) with the predicted medians by the AS16 model for the four events of Yangbi sequence, respectively. The empirical model of path duration for the active tectonic regions by (Boore and Thompson 2014; BT14) was also compared. (b) Values of intra-event residual δW_{es} against R_{rup} for D_{5-95} . Distance-binned means (squares) with one standard deviation (error bars) are plotted. The trend line of δW_{es} against R_{rup} was obtained from the linear regression based on data with $R_{rup} > 15$ km.

As the same with the PGA and PSAs, the intra-event residuals were also computed for D_{5-95} , as shown in Fig. 11b. The δW_{es} values in general fluctuate around zero and show no obvious trends with distance. We also linearly fitted the δW_{es} against R_{rup} based on data with $R_{rup} \geq 15$ km and obtained an approximate value of Δc_3 , -0.0005 , which quantitatively indicate the well-described distance scaling by the AS16 model.

6. Conclusions

Since May 18, 2021, a seismic sequence shook the Yangbi county, west part of Yunnan Province in southwest China. This Yangbi seismic sequence consists of four $M_S \geq 5.0$ earthquakes that occurred successively in a short time (i.e. the M_S 5.6 foreshock, the M_S 6.4 mainshock, the M_S 5.0 and M_S 5.2 aftershocks), and large numbers of small earthquakes. During the 2021 Yangbi sequence, the strong-motion and seismic intensity stations have obtained large numbers of ground-motion recordings. The recordings in the four earthquakes with $M_S \geq 5.0$ from the Yangbi sequence were analyzed in detail to characterize the source effects, distance decay, etc.

The velocity pulse-like waveform at station 53YBX and the asymmetrical distance decay in the SSE-NNW direction (much slower toward the SSE) in the M_S 6.4 mainshock seem to hint the occurrence of the asymmetrical source rupture. The source rupture directivity was estimated by fitting the azimuth-dependent residual terms with the rupture directivity function. According to the retrieved rupture directivity parameters (the predominant rupture direction and the rupture velocity), the M_S 6.4 mainshock shows the significantly asymmetrical bilateral rupture propagation, predominantly in the SSE direction with a rupture velocity of about 2.24 km/s. Meanwhile, the M_S 5.6 foreshock is also characterized by the asymmetrical bilateral rupture with predominant rupture propagation in the NW direction, and no dependence of residual terms on azimuth indicates the symmetrical rupture propagation in the other two events.

We further compared the PGA and PSAs from the four earthquakes with the predicted medians of the ASK14 and CY14 GMPEs developed as part of the NGA-West2 project. The negative inter-events residuals indicate the weaker source contributions to ground motions in the four Yangbi earthquakes compared with the global shallow crustal earthquakes. We also noted the earthquake type-dependent source contributions on short-period ground motions, that is, M_S 5.6 foreshock > M_S 6.4 mainshock > M_S 5.2 aftershock, consistent with the dependence of stress drop on earthquake type. The δB_e values in the M_S 5.0 aftershock are far below the level in the M_S 5.2 aftershock, which may be explained by the spatial and temporal distance to the mainshock, that is, the very weak source contributions on ground motions for the aftershocks very close to the mainshock in space and time. The intra-event residuals against distance and the positive values of adjustment coefficient Δc_3 reflect that the anelastic attenuations in the study region are weaker than those for China represented by the ASK14 and CY14 models. Finally, comparisons between the ground-motion significant durations and two empirical models (AS16 model for predicting significant duration and the BT14 model for empirically illustrating the ground-motion path duration) indicate the distance scaling of significant duration can be well described by both models.

7. Data and Resources

Strong-motion recordings at strong-motion stations in this study were derived from the China Strong Motion Network Center at the Institute of Engineering Mechanics, China Earthquake Administration; contact the email csmnc@iem.ac.cn for data application. Strong-motion recordings at seismic intensity stations in this study were derived from Yunnan Earthquake Agency; contact the email hxmjcw@163.com for data application. Ground-motion intensity measures calculated for the four $M_S \geq 5.0$ earthquakes during Yangbi seismic sequence were publicly available at <https://doi.org/10.6084/m9.figshare.20380428.v1> (last accessed July 2022). The earthquake epicenters, focal depths and surface-wave magnitude were derived from the China Earthquake Network Center (CENC; <http://www.ceic.ac.cn/history>, last accessed September 2021). The focal mechanisms in the Global Centroid Moment Tensor catalog were obtained from <https://www.globalcmt.org/CMTsearch.html> (last accessed September 2021). The slope-based V_{S30} values were available at <https://earthquake.usgs.gov/data/vs30/> (last accessed September 2021).



Disclosure Statement

No potential conflict of interest was reported by the author(s).

Funding

This work was supported by the National Key R&D Program of China [Grant No. 2019YFE0115700], the Scientific Research Fund of Institute of Engineering Mechanics, China Earthquake Administration [Grant No. 2021EEVL0103], Natural Science Foundation of Heilongjiang Province [Grant No. LH2020E021].

ORCID

Shengyin Qiang <http://orcid.org/0000-0002-7255-4956>

Hongwei Wang <http://orcid.org/0000-0001-9706-6230>

Ruizhi Wen <http://orcid.org/0000-0001-6381-9425>

References

- Abrahamson, N. A., and W. J. Silva. 1997. Empirical response spectral attenuation relations for shallow crustal earthquakes. *Seismological Research Letters* 68 (1):94–127. doi:[10.1785/gssrl.68.1.94](https://doi.org/10.1785/gssrl.68.1.94).
- Abrahamson, N. A., W. J. Silva, and R. Kamai. 2014. Summary of the ASK14 ground motion relation for active crustal region. *Earthquake Spectra* 30 (3):1025–55. doi:[10.1193/070913EQS198M](https://doi.org/10.1193/070913EQS198M).
- Afshari, K., and J. P. Stewart. 2016. Physically parameterized prediction equations for significant duration in active crustal regions. *Earthquake Spectra* 32 (4):2057–81. doi: [10.1193/063015EQS106M](https://doi.org/10.1193/063015EQS106M).
- Al Atik, L., N. Abrahamson, J. J. Bommer, F. Scherbaum, F. Cotton, and N. Kuehn. 2010. The variability of ground-motion prediction models and its components. *Seismological Research Letters* 81 (5):794–801. doi:[10.1785/gssrl.81.5.794](https://doi.org/10.1785/gssrl.81.5.794).
- Ameri, G., S. Drouet, P. Traversa, D. Bindi, and F. Cotton. 2017. Toward an empirical ground motion prediction equation for France: Accounting for regional differences in the source stress parameter. *Bulletin of Earthquake Engineering* 15 (11):4681–717. doi:[10.1007/s10518-017-0171-1](https://doi.org/10.1007/s10518-017-0171-1).
- Baltay, A. S., T. C. Hanks, and N. A. Abrahamson. 2019. Earthquake stress drop and Arias intensity. *Journal of Geophysical Research: Solid Earth* 124 (4):3838–52. doi:[10.1029/2018JB016753](https://doi.org/10.1029/2018JB016753).
- Ben-Menahem, A. 1961. Radiation of seismic surface-waves from finite moving sources. *Bulletin of the Seismological Society of America* 51 (3):401–35. doi: [10.1785/BSSA0510030401](https://doi.org/10.1785/BSSA0510030401).
- Bindi, D., S. Parolai, H. Grosser, C. Milkereit, and E. Durukal. 2007. Empirical ground-motion prediction equations for northwestern Turkey using the aftershocks of the 1999 Kocaeli earthquake. *Geophysical Research Letters* 34 (8). doi:[10.1029/2007GL029222](https://doi.org/10.1029/2007GL029222).
- Bindi, D., D. Spallarossa, and F. Pacor. 2017. Between-event and between-station variability observed in the Fourier and response spectra domains: Comparison with seismological models. *Geophysical Journal International* 210 (2):1092–104. doi:[10.1093/gji/ggx217](https://doi.org/10.1093/gji/ggx217).
- Boatwright, J. 2007. The persistence of directivity in small earthquakes. *Bulletin of the Seismological Society of America* 97 (6):1850–61. doi:[10.1785/0120050228](https://doi.org/10.1785/0120050228).
- Boore, D. M. 2005. On pads and filters: Processing strong-motion data. *Bulletin of the Seismological Society of America* 95 (2):745–50. doi:[10.1785/0120040160](https://doi.org/10.1785/0120040160).
- Boore, D. M. 2010. Orientation-independent, nongeometric-mean measures of seismic intensity from two horizontal components of motion. *Bulletin of the Seismological Society of America* 100 (4):1830–35. doi:[10.1785/0120090400](https://doi.org/10.1785/0120090400).
- Boore, D. M., and E. M. Thompson. 2014. Path durations for use in the stochastic-method simulation of ground motions. *Bulletin of the Seismological Society of America* 104 (5):2541–52. doi:[10.1785/0120140058](https://doi.org/10.1785/0120140058).
- Chen, J. L., J. L. Hao, Z. Wang, and T. Xu. 2022. The 21 May 2021 M_w 6.1 Yangbi earthquake—a unilateral rupture event with conjugately distributed aftershocks. *Seismological Research Letters* 93 (3):1382–99. doi:[10.1785/0220210241](https://doi.org/10.1785/0220210241).
- Chiou, B.-S.-J., and R. R. Youngs. 2014. Update of the Chiou and Youngs NGA model for the average horizontal component of peak ground motion and response spectra. *Earthquake Spectra* 30 (3):1117–53. doi:[10.1193/072813EQS219M](https://doi.org/10.1193/072813EQS219M).
- Douglas, J. 2021. Ground motion prediction equations 1964–2021. Department of Civil and Environmental Engineering, University of Strathclyde, UK. <http://www.gmpe.org.uk/gmpereport2014.pdf>.
- Duan, M., C. Zhao, L. Zhou, C. Zhao, and K. Zuo. 2021. Seismogenic structure of the 21 May 2021 M_s 6.4 Yunnan Yangbi earthquake sequence. *Chinese Journal of Geophysics* 64 (9):3111–25. doi:[10.6038/cjg2021P0423](https://doi.org/10.6038/cjg2021P0423). (in Chinese).
- Gao, M., ed. 2015. *Publicizing materials of GB 18306–2015 Chinese ground motion parameter zoning map*. Beijing, China: Standard Press of China. (in Chinese).

- Gong, W., L. Ye, T. Lay, H. Kanamori, and X. Chen. 2021. Rupture directivity of the May 21, 2021 M_W 6.0 Yangbi, Yunnan earthquake. *AGU Fall Meeting Abstracts*, New Orleans, LA, S55F-0213.
- Heath, D., D. J. Wald, C. B. Worden, E. M. Thompson, and G. M. Smoczyk. 2020. A global hybrid V_{s30} map with a topographic slope-based default and regional map insets. *Earthquake Spectra* 36 (3):1570–84. doi:[10.1177/8755293020911137](https://doi.org/10.1177/8755293020911137).
- Huangfu, G., Z. Li, J. Qin, and J. Zhang. 2007. Correlation of seismicity in Sichuan-Yunnan rhombic block. *Journal of Seismological Research* 30 (3):205–09. (in Chinese).
- Joyner, W. B. 1991. Directivity for non-uniform ruptures. *Bulletin of the Seismological Society of America* 81 (4):1391–95. doi:[10.1785/BSSA0810041391](https://doi.org/10.1785/BSSA0810041391).
- Kane, D. L., P. M. Shear, B. P. Goertz-Allmann, and F. L. Vernon. 2013. Rupture directivity of small earthquakes at Parkfield. *Journal of Geophysical Research: Solid Earth* 118 (1):212–21. doi:[10.1029/2012JB009675](https://doi.org/10.1029/2012JB009675).
- Konno, K., and T. Ohmachi. 1998. Ground-motion characteristics estimated from spectral ratio between horizontal and vertical components of microtremor. *Bulletin of the Seismological Society of America* 88 (1):228–41. doi:[10.1785/BSSA0880010228](https://doi.org/10.1785/BSSA0880010228).
- Laske, G., G. Masters, Z. Ma, and M. Pasyanos. 2013. Update on CRUST1.0 - A 1-degree global model of Earth's crust. *Geophysical Research Abstracts* 15:EGU2013–2658.
- Li, X., C. Zhai, W. Wen, and L. Xie. 2020. Ground motion prediction model for horizontal PGA, 5% damped response spectrum in Sichuan-Yunnan region of China. *Journal of Earthquake Engineering* 24 (11):1829–66. doi:[10.1080/13632469.2018.1485600](https://doi.org/10.1080/13632469.2018.1485600).
- Li, C., J. Zhang, W. Wang, K. Sun, and X. Shan. 2021. The seismogenic fault of the 2021 Yunnan Yangbi M_s 6.4 earthquake. *Seismology and Geology* 43 (3):706–21. (in Chinese).
- Long, F., Y. Qi, G. Yi, W. Wu, G. Wang, X. Zhao, and G. Peng. 2021. Relocation of the M_s 6.4 Yangbi earthquake sequence on May 21, 2021 in Yunnan Province and its seismogenic structure analysis. *Chinese Journal of Geophysics* 64 (8):2631–46. doi:[10.6038/cjg2021O0526](https://doi.org/10.6038/cjg2021O0526). (in Chinese).
- Lyu, H., and F. Zhao. 2007. Site coefficients suitable to China site category. *Acta Seismologica Sinica* 20 (1):71–79. doi:[10.1007/s11589-007-0071-6](https://doi.org/10.1007/s11589-007-0071-6).
- Moyer, P. A., M. S. Boettcher, J. J. McGuire, and J. A. Collins. 2018. Spatial and temporal variations in earthquake stress drop on gofar transform fault, east pacific rise: Implications for fault strength. *Journal of Geophysical Research: Solid Earth* 123 (9):7722–40. doi:[10.1029/2018JB015942](https://doi.org/10.1029/2018JB015942).
- Peng, C., P. Jiang, Q. Chen, Q. Ma, and J. Yang. 2019. Performance evaluation of a dense MEMS-based seismic sensor array deployed in the Sichuan-Yunnan border region for earthquake early warning. *Micromachines* 10 (11):735. doi:[10.3390/mi10110735](https://doi.org/10.3390/mi10110735).
- Ran, H., and G. Wu. 2019. Seismicity around late quaternary active faults in China. *Bulletin of the Seismological Society of America* 109 (4):1498–523. doi:[10.1785/0120180340](https://doi.org/10.1785/0120180340).
- Ren, Y., H. Wang, and R. Wen. 2017. Imprint of rupture directivity from ground motions of the 24 August 2016 M_w 6.2 Central Italy earthquake. *Tectonics* 36 (12):3178–91. doi:[10.1002/2017TC004673](https://doi.org/10.1002/2017TC004673).
- Ren, Y., H. Wang, P. Xu, Y. P. Dhakal, R. Wen, Q. Ma, and P. Jiang. 2018. Strong-motion observations of the 2017 M_s 7.0 Jiuzhaigou earthquake: Comparison with the 2013 M_s 7.0 Lushan earthquake. *Seismological Research Letters* 89 (4):1354–65. doi:[10.1785/0220170238](https://doi.org/10.1785/0220170238).
- Sgobba, S., G. Lanzano, and F. Pacor. 2021. Empirical nonergodic shaking scenarios based on spatial correlation models: An application to central Italy. *Earthquake Engineering Structural Dynamics* 50 (1):60–80. doi:[10.1002/eqe.3362](https://doi.org/10.1002/eqe.3362).
- Shahi, S. K., and J. W. Baker. 2014. An efficient algorithm to identify strong-velocity pulses in multicomponent ground motions. *Bulletin of the Seismological Society of America* 104 (5):2456–66. doi:[10.1785/0120130191](https://doi.org/10.1785/0120130191).
- Smith, W. H. F., and P. Wessel. 1990. Gridding with continuous curvature splines in tension. *Geophysics* 55 (3):293–305. doi:[10.1190/1.1442837](https://doi.org/10.1190/1.1442837).
- Trifunac, M. D., and A. G. Brady. 1975. A study on the duration of strong ground motion. *Bulletin of the Seismological Society of America* 65 (3):581–626. doi:[10.1785/BSSA0650030581](https://doi.org/10.1785/BSSA0650030581).
- Trugman, D. T., and P. M. Shearer. 2018. Strong correlation between stress drop and peak ground acceleration for recent M 1-4 earthquakes in the San Francisco Bay area. *Bulletin of the Seismological Society of America* 108 (2):929–45. doi:[10.1785/0120170245](https://doi.org/10.1785/0120170245).
- Wang, H., and R. Wen. 2021. Attenuation and basin amplification revealed by the dense ground motions of the 12 July 2020 M_s 5.1 Tangshan, China, Earthquake. *Seismological Research Letters* 92 (4):2109–21. doi:[10.1785/0220200400](https://doi.org/10.1785/0220200400).
- Wen, R., H. Wang, and Y. Ren. 2015. Rupture directivity from strong-motion recordings of the 2013 Lushan aftershocks. *Bulletin of the Seismological Society of America* 105 (6):3068–82. doi:[10.1785/0120150100](https://doi.org/10.1785/0120150100).
- Xu, X., X. Wen, R. Zheng, W. Ma, F. Song, and G. Yu. 2003. Pattern of latest tectonic motion and its dynamics for active blocks in Sichuan-Yunnan region, China. *Science in China Series D: Earth Sciences* 46:210–26. doi:[10.1360/03dz0017](https://doi.org/10.1360/03dz0017).
- Yang, J., Y. Wen, and C. Xu. 2021. The 21 May 2021 M_s 6.4 Yangbi (Yunnan) earthquake: A shallow strike-slip event rupturing in a blind fault. *Chinese Journal of Geophysics* 64 (9):3101–10. doi:[10.6038/cjg2021P0408](https://doi.org/10.6038/cjg2021P0408). in Chinese.
- Yu, Y., S. Li, and L. Xiao. 2013. Development of ground motion attenuation relations for the new seismic hazard map of China. *Technology for Earthquake Disaster Prevention* 8 (1):24–33. (in Chinese).